BLEDAR: Bluetooth LE Direction and Ranging Fused with Inertial Sensing for GNSS-denied Navigation

Kristoffer Gryte[1,#], Glen Hjelmerud Mørkbak Sørensen[1,#], Johan Suárez[2], Torleiv H. Bryne[1], Kimmo Kansanen[2] and Tor Arne Johansen[1]

***Abstract*—We demonstrate a fully Bluetooth Low Energy (BLE)-based phased-array radio system (PARS)-aided GNSS-denied navigation system using a single ground-based sensor unit. We apply a Bayesian estimation framework to obtain range measurements from the raw tones of BLE channel sounding measurements, outperforming the conventional IFFT-based methods, and use them alongside azimuth and elevation measurements obtained using BLE Direction Finding. The PARS measurements are fused with inertial sensor data using a factor graph optimisation (FGO) algorithm with robust cost functions to handle outliers. We compare the navigation performance with that of a 5-anchor ultra wideband (UWB) multiranging system, which we consider to be a comparable navigation system in terms of cost and commercial availability, but requires more infrastructure.**

***Index Terms*—Bluetooth LE, phased-array radio systems, GNSS-denied navigation, phase-based ranging, factor graph optimisation**

I. Introduction

Global navigation satellite systems (GNSS) fused with inertial navigation systems (INS) is the classic approach for global navigation across domains and platforms navigating under open skies. However, GNSS is highly vulnerable to radio frequency interference (RFI) due to its low signal power [1]. There are several alternatives to GNSS-denied navigation using e.g., camera-based methods such as visual odometry [2], visual simultaneous localisation and mapping (VSLAM), and Lidar SLAM [3]. However, these all struggle in visually degraded and/or self-similar environments, such as when flying over water. An option to address this potential problem is local radio-based navigation.

In previous work, fusion of range and bearing measurements from a commercial phased-array radio system (PARS) with measurements using an inertial measurement unit (IMU) has been the focus [4], [5]. A unique advantage with such a system is the ability to resolve the 3D position of a vehicle from a single antenna array, which could simplify deployment compared to deploying three or more anchors for multi-ranging.

With the introduction of direction finding (DF) to the Bluetooth 5.1 standard in 2019, phase-based localisation was made available at low cost, primarily due to cheap, mass produced components and a design with a single transmitter/receiver that switches between the antennas in the array. Bluetooth Low Energy (BLE) DF supports angle-of-arrival (AoA) estimation, where the anchor transmits a signal to one or more arrays that estimate the arrival angles of the incoming signals.

There is a vast literature on algorithms for DF, see e.g., [6], [7], we use direct data acquisition of propagators (PDDA) [8] for its simplicity. The three-dimensional position of the transmitter can be found from multiranging, which requires multiple arrays. Since it is narrow-band, multipath is particularly challenging for Bluetooth. The reflected wave interferes with the direct wave, which materialises as coloured noise in the DF estimates. Effects on DF and mitigation of NLOS and multipath are shown in [9].

Bluetooth has indirectly supported range estimation via received signal strength and round-trip timing (RTT). However, for many applications the accuracy obtained with these ranging techniques is not sufficient to provide a meaningful 3D position estimate from a single range measurement combined with a single antenna array and phase-based DF.

In 2024, Channel Sounding (CS) was introduced in the Bluetooth 6.0 release [10]. CS supports both Phase-based Ranging (PBR) and Round-Trip Timing (RTT) distance measurement methods [11]. The specification standardises CS execution at the controller level, but leaves data processing and performance optimisation to the implementer. To this end, multiple algorithms have been developed that perform ranging using phase measurements. Since the phase variation between frequencies depends linearly on the propagation distance, it is possible to measure range by phase measurements [12]. Two-way measurements allow for elimination of phase offsets and ambiguities, enabling unambiguous range over a maximum distance determined by the frequency spacing. Algorithms such as Multicarrier Phase Difference (MCPD), FFT-based methods, and super-resolution-based methods have demonstrated centimetre-level accuracy on commercial hardware

The authors are with the [1]Department of Engineering Cybernetics and [2] Department of Electronic Systems, Norwegian University of Science and Technology (NTNU), NO-7491 Trondheim, Norway. Corresponding authors e-mail: {kristoffer.gryte,glen.h.m.sorensen}@ntnu.no

Kristoffer Gryte[#] and Glen Hjelmerud Mørkbak Sørensen[#] contributed equally to this work and should be considered co-first authors.

The work is supported by the Research Council of Norway through the project Phased-array radio systems for resilient localization and navigation of autonomous systems in GNSS-denied environments PARNAV (No. 338789), and Multi-Sensor Data Timing, Synchronization and Fusion for Intelligent Robots (SentiPro), no. 327538.

[13]–[15]. Furthermore, [16] and [17] evaluate the performance of different estimators against the Cramér–Rao bound. The results in [16] indicate that the estimation based on IFFT achieves the lowest mean squared error (MSE) amongst classical estimation methods. In [17], a Bayesian estimator is proposed that reaches the modified Cramér–Rao bound at high signal-to-noise radio (SNR) and outperforms existing estimators by approximately 6 dB.

A. Main contribution

Various research has demonstrated the potential for localisation using BLE CS or DF [16]–[18]. [19] has used DF in a navigation system and fused DF estimates (azimuth and elevation) with inertial measurement unit (IMU) data. However, [19] did not use the CS-based range estimates to aid the INS. To the best of our knowledge, we are the first to demonstrate the fusion of both CS and DF measurements with inertial sensors to obtain a fully BLE-based PARS (BLEDAR)-aided GNSS-denied navigation system using a single ground-based sensor unit. The PARS measurements are fused with IMU measurements using factor graph optimisation (FGO) in a tightly coupled manner, as opposed to the error state Kalman filter used in [4], [5].

We investigate navigation performance in a practical outdoor environment navigating a multirotor unmanned aerial systems (UAS), where the only source of position is range, azimuth, and elevation PARS measurements. The phase-based range is computed using a Bayesian estimator [17]. We compare the navigation performance with that of a 5-anchor ultra wideband (UWB) multiranging system, which we consider to be a comparable navigation system in terms of cost and commercial availability, but requires more infrastructure. We also add barometer aiding to the navigation system to improve overall performance when PARS measurements degrade due to NLOS, multipath or low SNR. We consider the estimates from an FGO with real-time kinematics (RTK)-GNSS position measurements as the ground truth position reference. The core FGO and IMU measurements are the same in the three configurations.

II. Preliminaries

Vectors and matrices are given in lowercase and uppercase bold-fond letters, $\boldsymbol{v}$ and $\boldsymbol{V}$, respectively. $[\boldsymbol{a}]_\times$ denotes the skew-symmetric matrix of a 3D vector $\boldsymbol{a}$, $\| \bullet \|$ denotes the Euclidean norm of a vector, whilst $| \bullet |$ denotes the norm of a complex number. The transpose and complex conjugate are given by $\boldsymbol{v}^\top$ and $\boldsymbol{v}^\mathrm{H}$, respectively. We consider three coordinate frames, as illustrated in Fig. 1 and described below:

- The local North-East-Down (NED) navigation frame $\{n\}$ that has its origin in the centre of the PARS ground antenna array,
- the BODY-fixed frame $\{b\}$ that has its origin at the BLE transmitter antenna on the robot, and
- the BLE PARS radio frame $\{r\}$ that has the same origin as NED, but with axes aligned with the PARS antennas.

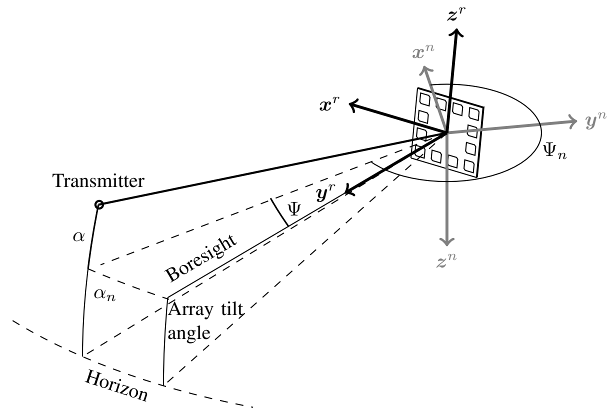

Fig. 1. Illustration of array setup with coordinate frames $\{r\}$ and $\{n\}$, and the angle notation used for directions from the array. Ψ is the azimuth angle. α is the elevation angle. $\boldsymbol{y}^r$ is the boresight direction, which is the direction where the antenna elements have the maximum gain. $\boldsymbol{x}^n$ is the North direction and Ψ_n is the heading angle to the transmitter relative North.

With this notation, $\boldsymbol{p}^n_{rb}$ describes the position from $\{r\}$ to $\{b\}$ expressed in $\{n\}$.

A. Bluetooth Low Energy Direction finding

BLE DF relies on a constant tone extension (CTE) period that is appended to regular BLE advertisement packet before transmission. This CTE is a sequence of unwhitened binary ones which results in a fixed-frequency sine wave being transmitted. For AoA estimation, the receiver samples the array by switching through the elements in a pre-determined switching pattern throughout the CTE period. For DF we define the azimuth (Ψ) and elevation angle (α) of the incoming signal as illustrated in Fig. 1. For more details, see, e.g., [18]. Since sampling is done whilst switching between antenna array elements in sequence (not simultaneously), it is convenient to assume that there is a constant bearing between the tag/transmitter and the DF antenna array over the CTE period.

To estimate the angles Ψ and α from the measured baseband signal $\boldsymbol{x}(t) = \boldsymbol{i}(t) + j\boldsymbol{q}(t) \in \mathbb{C}^m$ from a single source, we employ the following measurement model [20]:

$$\boldsymbol{x}(t) = \boldsymbol{a}(\Psi, \alpha)s(t) + \boldsymbol{n}(t). \tag{1}$$

Here, $s(t) \in \mathbb{C}$ is the transmitted baseband signal waveform, $\boldsymbol{n}(t) \in \mathbb{C}^m$ is additive noise and

$$\boldsymbol{a}(\Psi, \alpha) = e^{\frac{2\pi j}{\lambda} \boldsymbol{P}^{a\top} \boldsymbol{l}(\Psi,\alpha)} \in \mathbb{C}^m, \tag{2}$$

is the far-field/plane wave steering vector, λ is the wavelength of the signal, and $\boldsymbol{P}^a$ is the matrix of array antenna positions

$$\boldsymbol{P}^a = \left[\boldsymbol{p}^a_1, \dots, \boldsymbol{p}^a_m\right] \in \mathbb{R}^{3\times m}, \tag{3}$$

and the line-of-sight direction unit vector is expressed as

$$\boldsymbol{l}(\Psi, \alpha) = \begin{bmatrix} \sin(\Psi)\cos(\alpha) \\ \cos(\Psi)\cos(\alpha) \\ \sin(\alpha) \end{bmatrix}, \tag{4}$$

as illustrated in Fig. 1.

Before further processing, the drift caused by the carrier frequency offset (CFO) between transmitter and receiver must be compensated. Similarly to [18], the CFO is estimated using all the data from the CTE. The corrected IQ measurements $\bar{\boldsymbol{x}}$ from the full CTE are assumed to be simultaneous, before they are used to compute the pseudo-spectrum from

$$P(\Psi, \alpha) = |\boldsymbol{a}(\Psi, \alpha)^{\mathrm{H}} \bar{\boldsymbol{x}}|^2. \tag{5}$$

The estimated azimuth and elevation cf. (4), $\hat{\Psi}$ and $\hat{\alpha}$, correspond to the peak of $P(\Psi, \alpha)$, which are estimated through a coarse and a fine search.

B. Bluetooth Low Energy Channel Sounding

Channel Sounding operates in the 2.4 GHz Industrial, Scientific, and Medical (ISM) band, similarly to conventional Bluetooth and BLE systems. It employs a channelisation scheme consisting of 80 channels with 1 MHz spacing. For phase-based ranging, this spacing determines the unambiguous distance, $d_{\text{max}} = \frac{c}{2\Delta f}$, which for $\Delta f = 1\,\text{MHz}$ corresponds to approximately 150 m [12].

In this work we only use PBR to estimate range. To avoid interference with BLE advertising channels (37, 38, and 39), overlapping frequencies are excluded from operation. As a result, 72 out of the 80 defined channels are available for Channel Sounding measurements [21].

Phase-based ranging measurements are based on the active reflector principle, which has been extensively studied in prior work [13], [14], [17], [22]. In essence, the Initiator and Reflector exchange single-tone signals to estimate the bidirectional channel frequency response (CFR), yielding a two-way CFR measurement. Specifically, the Initiator transmits a tone at frequency f_k, selected from a predefined set of K_f channels uniformly spaced at Δ_f. At the receiver side, the Reflector measures the phase and responds with a tone at the same frequency whilst also transmitting the corresponding one-way measured CFR to the Initiator. After this exchange the Initiator has both CFRs. The procedure is repeated over K_f frequencies.

The collected CFRs consist of a pair of complex baseband observations for each tone:

$$\tilde{y}_{R,k} = a_{R,k} e^{j\theta_{R,k}} = x_{R,k} + w_{R,k}, \tag{6}$$
$$\tilde{y}_{I,k} = a_{I,k} e^{j\theta_{I,k}} = x_{I,k} + w_{I,k}, \tag{7}$$

where the subindex I and R refer to Initiator and Reflector, respectively, and k is the frequency index. The noiseless signals $x_{R,k}$ and $x_{I,k}$ are modelled as

$$x_{R,k} = a_R e^{j(-2\pi\Delta_f(\rho/c_0) + \Delta\phi_k)}, \tag{8}$$
$$x_{I,k} = a_I e^{j(-2\pi k\Delta_f(\rho/c_0) - \Delta\phi_k)}, \tag{9}$$

where a_R and a_I are the amplitudes of the transmitted tones, k the tone index, Δ_f the space between tones, ρ the distance between the radio units, c_0 is the speed of light, and $\Delta\phi_k$ accounts for both small epoch misalignments between the transceivers and the phase offset arising from their local oscillators. Finally, $w_R(f_k) \sim \mathcal{N}(0, \sigma_0^2)$ and $w_I(f_k) \sim \mathcal{N}(0, \sigma_0^2)$ denote the white Gaussian noise at the Reflector and Initiator, respectively, with variance σ_0^2. The noise is assumed i.i.d. between the Reflector and Initiator, and across different tones. The signal model assumes a constant ρ, i.e., both radios remain static throughout the measurement procedure, and may be inaccurate at higher drone velocities.

We estimate the range using the Bayesian algorithm described in [17]. The range is found by

$$\hat{\rho} = \arg\max_{\rho} M(\rho), \tag{10}$$

where the metric is computed with

$$M(\rho) = \sum_{k=1}^{K_f} \log I_0 \left(2\cos\left(-\frac{2\pi f_k \rho}{c_0} - \frac{\theta_{R,k} + \theta_{I,k}}{2} \right) \right), \tag{11}$$

where $I_0(\bullet)$ denotes the modified Bessel function of the first kind. As the metric (11) is multimodal, a variant of the Local-to-Global Maximum Search (LGMS) algorithm is used to identify the global maximum. Following [17], the search is initialised using the IFFT-based estimator [14], and a gradient-based search is applied to ensure convergence to a local maximum. Subsequently, the metric is evaluated at offsets of ± 2.4m from this first estimate and over the interval from zero to the maximum unambiguous range. The three largest candidate values are selected, and each is further refined using a gradient-based local search. The index corresponding to the highest refined value is returned as the distance estimate, representing the global maximum of the metric.

III. Integrated Navigation System

The integrated navigation system is an extension of that found in [19] and is an INS aided by BLE PARS and GNSS measurements based on incremental fixed delay smoother (iSAM2) [23] found in the GTSAM C++ framework for FGO [24]. I.e., fusing IMU, GNSS, and BLE PARS measurements. It estimates the state of the robot pose, velocity, and IMU biases on the form $\hat{\boldsymbol{x}} \triangleq (\hat{\boldsymbol{T}}_b^n,\ \hat{\boldsymbol{v}}_{nb}^n,\ \hat{\boldsymbol{b}}_b) \in SE(3) \times \mathbb{R}^3 \times \mathbb{R}^6$, where the matrix Lie group $SE(3)$ is defined as the set of poses $\boldsymbol{T} \in \mathbb{R}^{4\times4}$

$$SE(3) \triangleq \left\{ \boldsymbol{T} = \begin{bmatrix} \boldsymbol{R} & \boldsymbol{p} \\ \boldsymbol{0}_{1\times3} & 1 \end{bmatrix} \middle| \begin{array}{l} \boldsymbol{R} \in SO(3), \\ \boldsymbol{p} \in \mathbb{R}^3 \end{array} \right\}, \tag{12}$$

where $\boldsymbol{R} \in SO(3)$ is a 3×3 rotation matrix, which is itself part of the $SO(3)$ matrix Lie group [25], and $\boldsymbol{p}$ is a position vector.

The fixed-lag smoother is configured with a smoother lag of 5 seconds with a re-linearisation threshold of 0.001 and to use QR for numerical factorisation.

A. On-manifold IMU preintegration

The state prediction between the navigation system's measurement updates is driven by the on-manifold IMU preintegrator found in GTSAM [26]–[28] which use the information from accelerometer and gyroscope measurements between time steps i and j as

$$\begin{aligned} \Delta\tilde{\boldsymbol{R}}_{ij} &= \boldsymbol{R}_i^\top \boldsymbol{R}_j \mathrm{Exp}\left(\boldsymbol{w}_o\right) \\ \Delta\tilde{\boldsymbol{v}}_{ij} &= \boldsymbol{R}_i^\top (\boldsymbol{v}_j - \boldsymbol{v}_i - \boldsymbol{g}\Delta t_{ij}) + \boldsymbol{w}_v \\ \Delta\tilde{\boldsymbol{p}}_{ij} &= \boldsymbol{R}_i^\top (\boldsymbol{p}_j - \boldsymbol{p}_i - \boldsymbol{v}_i\Delta t_{ij} - \frac{1}{2}\boldsymbol{g}\Delta {t_{ij}}^2) + \boldsymbol{w}_p, \end{aligned} \tag{13}$$

where $\boldsymbol{w}_o$, $\boldsymbol{w}_v$, and $\boldsymbol{w}_p$ are gyroscope, accelerometer, and preintegration white noise, respectively.

B. Measurement models and factors

All factors need its Jacobian before they can be added to the graph prior to optimisation. These are defined with respect to the Lie algebra $\mathfrak{se}(3)$ where the *local perturbation* $\boldsymbol{\xi}$ is defined as

$$\boldsymbol{\xi} \triangleq \begin{bmatrix} {\boldsymbol{\xi}_o}^\top & {\boldsymbol{\xi}_p}^\top \end{bmatrix}^\top \in \mathbb{R}^6, \tag{14}$$

which can be expressed on the Lie algebra using the *hat operator* $^\wedge$ [25]:

$$\mathfrak{se}(3) \triangleq \left\{ \boldsymbol{\xi}^\wedge = \begin{bmatrix} [\boldsymbol{\xi}_o]_\times & \boldsymbol{\xi}_p \\ \boldsymbol{0}_{1\times 3} & 0 \end{bmatrix} \middle| \begin{array}{l} [\boldsymbol{\xi}_o]_\times \in \mathfrak{so}(3), \\ \boldsymbol{\xi}_p \in \mathbb{R}^3 \end{array} \right\}, \tag{15}$$

where $\boldsymbol{\xi}_o$ and $\boldsymbol{\xi}_p$ are small increments in rotation and translation expressed in $\{b\}$, respectively. The Jacobians were found by the chain rule

$$\frac{\partial h_\bullet}{\partial \boldsymbol{\xi}^\wedge} = \frac{\partial h_\bullet}{\partial \boldsymbol{p}_{rb}^n} \frac{\partial \boldsymbol{p}_{rb}^n}{\partial \boldsymbol{\xi}^\wedge}, \tag{16}$$

where $h_\bullet$ represents one of the measurements in (18) (i.e., $z_\bullet = h_\bullet(x) + \varepsilon_\bullet$).

1) RTK-GNSS: In an initial stabilisation period, the multirotor is aided by RTK-GNSS position measurements, with measurement model and Jacobian $\boldsymbol{H}_\bullet$, given by

$$\boldsymbol{z}_{\text{RTK}}^n = \boldsymbol{p}_{nb}^n + \boldsymbol{\varepsilon}, \tag{17a}$$

$$\boldsymbol{h}_{\text{RTK}}(\hat{\boldsymbol{T}}) = \hat{\boldsymbol{p}}_{nb}^n, \tag{17b}$$

$$\boldsymbol{H}_{\text{RTK}} = \begin{bmatrix} \boldsymbol{0}_{3\times 3} & \hat{\boldsymbol{R}}_b^n \end{bmatrix}, \tag{17c}$$

where $\boldsymbol{l}_{\text{RTK}}^b$ is the RTK-GNSS baseline between two GNSS antennas on the multirotor.

2) BLE PARS: Similar to previous work [4], [19], [29], we use the PARS measurement model below

$$\boldsymbol{z}_{\text{PARS}}^r = \begin{bmatrix} \hat{\rho}^r \\ \hat{\Psi}^r \\ \hat{\alpha}^r \end{bmatrix} = \begin{bmatrix} \|\boldsymbol{p}_{rb}^r\|_2 + \varepsilon_\rho \\ \text{arctan2}\left(p_{rb,y}^r, p_{rb,x}^r\right) + \varepsilon_\Psi \\ \text{arctan2}\left(-p_{rb,z}^r, \hat{\rho}^r\right) + \varepsilon_\alpha \end{bmatrix}, \tag{18}$$

where $\boldsymbol{\varepsilon}_\bullet$ represent zero-mean Gaussian noise and $\hat{\rho}^r$, $\hat{\Psi}^r$, and $\hat{\alpha}^r$ are the range, azimuth angle, and elevation angle measurements expressed in $\{r\}$, respectively, estimated using DF and CS.

Based on the measurement model (18) and the chain-rule (16), the resulting PARS Jacobians are

$$\boldsymbol{H}_\rho = \frac{1}{\|\hat{\boldsymbol{p}}_{rb}^r\|_2} (\hat{\boldsymbol{p}}_{rb}^r)^\top \boldsymbol{H}_p \tag{19a}$$

$$\boldsymbol{H}_\Psi = \frac{1}{\hat{p}_x^2 + \hat{p}_y^2} \begin{bmatrix} -\hat{p}_y & \hat{p}_x & 0 \end{bmatrix} \boldsymbol{H}_p \tag{19b}$$

$$\boldsymbol{H}_\alpha = \frac{1}{\|\hat{\boldsymbol{p}}_{rb}^r\|_2^2} \begin{bmatrix} \frac{p_x p_z}{\sqrt{\hat{p}_x^2 + \hat{p}_y^2}} & \frac{p_y p_z}{\sqrt{\hat{p}_x^2 + \hat{p}_y^2}} & -\sqrt{\hat{p}_x^2 + \hat{p}_y^2} \end{bmatrix} \boldsymbol{H}_p, \tag{19c}$$

as in [19], where $\boldsymbol{H}_p$ is essential to relate the measurements to the Lie algebra and the position error. This was done in [19], [29] via the first-order approximation:

$$\boldsymbol{p}_{rb}^r \approx \hat{\boldsymbol{p}}_{rb}^r + \frac{\partial \boldsymbol{p}_{rb}^r}{\partial \boldsymbol{\xi}^\wedge}\boldsymbol{\xi} = \hat{\boldsymbol{p}}_{rb}^r + \boldsymbol{H}_p\boldsymbol{\xi}, \tag{20}$$

resulting in the group Jacobian

$$\boldsymbol{H}_p = [\boldsymbol{0}_3 \ (\boldsymbol{R}_r^n)^\top \hat{\boldsymbol{R}}_b^n], \tag{21}$$

relating the measurement expressed in $\{r\}$ to $\mathfrak{se}(3)$.

C. UWB range factors

When using the UWB for comparison to the BLE PARS system, we use the following measurement model

$$\boldsymbol{z}_{\text{UWB,k}} = \|\boldsymbol{p}_{nb}^n - \boldsymbol{p}_{nu_k}^n\|_2 + \varepsilon_{\rho_k} \tag{22}$$

$$h_{\text{UWB}_k}(\hat{\boldsymbol{T}}) = \|\hat{\boldsymbol{p}}_{nb}^n - \boldsymbol{p}_{nu_k}^n\|_2, \tag{23}$$

with Jacobians

$$\boldsymbol{H}_{\rho_k} = \frac{1}{\|\hat{\boldsymbol{p}}_{nb}^n - \boldsymbol{p}_{nu_k}^n\|_2} (\hat{\boldsymbol{p}}_{rb}^r - \boldsymbol{p}_{nu_k}^n)^\top \boldsymbol{H}_p \tag{24}$$

$$\boldsymbol{H}_p = [\boldsymbol{0}_3 \ \hat{\boldsymbol{R}}_b^n], \tag{25}$$

where u_k represents the position of the k-th UWB anchor.

D. Barometric factor

We also used a barometer to provide vertical corrections with a factor based on the GTSAM's internal barometric factor. Instead of using GTSAM's two-way factor, also estimating the barometer bias effect on the height, we calculate the pressure bias and statically compensate for this before take-off directly to the pressure measurement. The modified factor is given as:

$$z_{\text{baro}} = \frac{\frac{p_{\text{baro,comp}}}{101.29}^{1/5.256} \cdot 288.08 - 288.14}{-0.00649} + \varepsilon_{\text{baro}} \tag{26a}$$

$$p_{\text{baro,comp}} = p_{\text{baro}} - b_{\text{baro}} \tag{26b}$$

$$\hat{z} = \begin{bmatrix} 0 & 0 & -1 \end{bmatrix} \hat{\boldsymbol{p}}_{nb}^n \tag{26c}$$

$$\boldsymbol{H}_{\text{baro,SE(3)}} = \begin{bmatrix} \boldsymbol{0}_{1\times 3} & \begin{bmatrix} 0 & 0 & 1 \end{bmatrix} \hat{\boldsymbol{R}}_b^n \end{bmatrix} \tag{26d}$$

where $\varepsilon_{\text{baro}}$ is zero-mean Gaussian noise. p_{baro} is the barometric pressure measurement given in kPa and calculated using

$$p_{\text{ref}} = p_0 \exp\left(\frac{Mgh}{RT}\right) \tag{27}$$

$$b_{\text{baro}} = p_{\text{baro,avg init}} - p_{\text{ref}} \tag{28}$$

where p_0 is the pressure in kPa at mean sea level, $M = 0.028\,96\,\mathrm{kmol}^{-1}$, $g = 9.806\,65\,\mathrm{m\,s}^{-2}$, h is the altitude above mean sea level before launch, $R = 8.3144\,\mathrm{J/(molK)}$ being the universal gas constant and T is the temperature. Eq. (26a) is based on the Earth atmosphere model [30] similar to GTSAM's internal barometric factor.

E. Geman Mc-Clure M-estimator for outlier mitigation

We use the generalised Geman-McClure M-estimator from [31], being a robust cost function, to mitigate the effect of outliers in the BLE PARS measurements. It is described by its cost function

$$Q_{\mathrm{G}}(\tilde{z}) = \frac{1}{2}\frac{c^2\tilde{z}^2}{c^2+\tilde{z}^2}, \tag{29}$$

where c is its threshold value and $\bar{z}$ is a residual between predicted and observed measurement. Whenever $\bar{z} \leq c$, its behaviour will be close to a least-squares estimator, but it aggressively de-weights outliers outside the threshold. The smoothness of the objective makes it suitable for real-time operations, but a potential drawback is that it may remove nearly all useful information if the measurement source is noisy. Potential mitigations may be using a more lenient threshold for noisier elevation angle measurements, since these are more prone to multipath effects, to retain sufficient information to keep the estimation problem observable.

IV. Experiment Setup

The multirotor UAS flight experiment data were obtained from an experimental campaign at one of NTNU's test sites near Trondheim. The multirotor flight pattern for the experiment is shown in the North–East plane in Fig. 2. The experiment was conducted as a sequence of level horizontal flights at fixed altitudes, with altitude changes occurring only between segments. The RTK range in Fig. 6 provides a proxy for these altitude steps. The experimental setup consisting of the multirotor payload in Fig. 3, as well as the ground station in Fig. 4, is shown in Fig. 5.

Both the payload and the ground station are equipped with a Raspberry Pi 4B single-board computer, the Sentisystems Sentiboard v1.3 for sensor interfacing and logging, Nordic Semiconductor nRF52833 development kits (devkits) for DF, and Nordic Semiconductor nRF54L15 development kits for CS with the external omnidirectional patch antenna Stingray WA.500w from Taoglas.

The multirotor is also equipped with two uBlox ZED-F9P GNSS receivers that are configured as rover and moving base as an accurate reference for comparison (ground truth). The STIM300 tactical grade IMU provides delta velocities and delta angles inertial measurements together with temperature. The multirotor flies a pre-programmed plan, controlled using ArduCopter v4.6.0 running on a Pixhawk Cube Orange autopilot that navigates independently, using its own GNSS-based sensor suite. However, we also supplement the PARS-based aided INS with the MS5611 barometric pressure sensor from the autopilot.

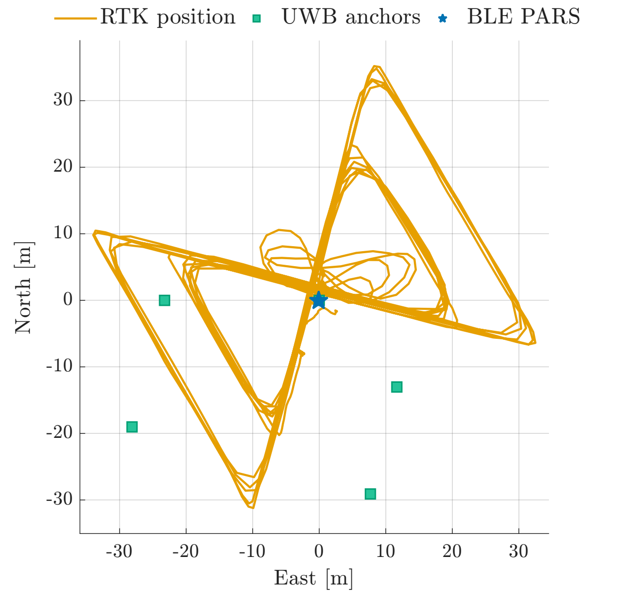

Fig. 2. RTK-GNSS-based flight pattern of multirotor UAS in North-East plane. The squares denote the positions of the UWB anchors, whilst the star denotes the position of the co-located PARS array and UWB anchor

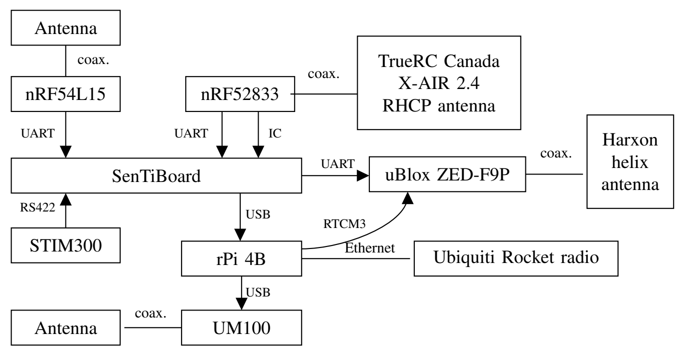

Fig. 3. UAS payload hardware schematic, adapted from [18].

The ground setup has a uBlox ZED-F9P GNSS receiver that both receives RTCM corrections from our fixed base station and sends RTCM corrections to the moving base GNSS receiver in the drone. The ground DF devkit is connected to a 12-element antenna array with truncated corner right-handed circular polarisation (RHCP) patch antenna elements in a $15 \times 15\,\mathrm{cm}$ frame pattern, with $5\,\mathrm{cm}$ antenna spacing. The time of arrival of the DF IQ samples from the ground DF

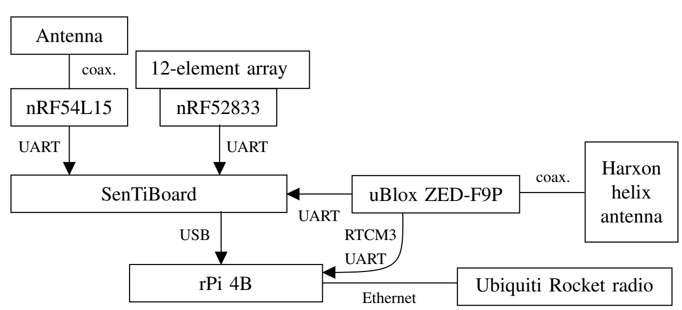

Fig. 4. Ground hardware schematic, adapted from [18].

Fig. 5. Multirotor UAS on the take-off stand, above the ground station with the 12-element antenna array and the CS antenna. The directional antenna on the UAS used for DF is seen in white, mounted in the front of the grey payload box. The smaller box in the lower right corner is a UWB anchor. After take-off, the wooden stand was moved.

TABLE I
NOMINAL MEASUREMENT RATES.

Sensor	Rate
IMU	2000 Hz
RTK GNSS	1 Hz
DF azimuth & elevation	$16-17$ Hz
CS range	0.5 Hz
Barometer pressure	10 Hz
UWB range	10 Hz

devkit lags behind the time of validity, when the signal was sent from the drone. To synchronise the DF IQ samples with the IMU and the other drone-side sensors, the drone-side DF devkit associates every CTE with a counter that is transmitted to the ground station in the BLE data packet associated with the CTE. When the CTE is sent, the devkit toggles a GPIO pin. This is detected and timestamped by the SenTiBoard. Then the IQ samples are associated with their time of validity (TOV) through the counter which is logged both on the ground and in the drone.

The drone is also equipped with a BeSpoon UM100 UWB tag, which performs range measurements against five anchors placed on the ground, see Fig. 2.

The nominal measurement rates of the multirotor sensor suite are given in Table I. The UWB ranges rates vary significantly in practice due to coverage differences for individual beacons. The DF devkits run custom firmware based on the Nordic Semiconductor's DF connectionless sample code [32] [33], with version 3.1 of the nRF Connect SDK (NCS). The modifications include

- Using the Zephyr Bluetooth soft device, to allow for 16 bit IQ samples.
- Using additional 8dB transmit power.
- Robustification to minimise downtime spent finding the transmission source in the event that the multirotor temporarily moves outside the array's range.
- Optimised CTE length and antenna array switching pattern, to improve CFO estimation, see [18].

Similarly, the CS devkits run a version of the Nordic Semiconductors connection-based channel sounding sample [34] for NCS v3.1, which has been robustified and adapted to lower SNR scenarios by increasing the minimum- and maximum subevent lengths at the cost of higher update rates in high SNR environments.

When performing DF with the Zephyr soft device, all data channels (0-36) are used to send CTEs, whilst channel sounding uses the 80 channels mentioned above in the same band with $1\,\mathrm{MHz}$ spacing. Consequently, there is a risk of collisions, i.e., self-interference when performing CS ranging and DF broadcasting simultaneously. However, given that DF uses pseudo-random channel hopping through the Channel Selection Algorithm (CSA) 2 [11], the chance of collision is acceptably small. To further reduce the risk of collision, CS could use CSA 3b (pseudo-random hopping) instead of CSA 3c (linear sweep), see [11], which could also improve the accuracy of the range [35]. In a more integrated BLE navigation stack, DF and CS could be separated in time or set to use different channels, to potentially improve overall performance.

The rotation between $\{r\}$ and $\{n\}$ was determined by applying the Fast Optimal Matrix Algorithm (FOAM) [36] using BLE DF and RTK range together with RTK position measurements. Similarly to [19], the RTK range information was used in this calibration to avoid the risk of outliers in the CS-based range estimates adversely affecting the estimation of antenna array mounting angles.

The tuning parameter for the aided INS, the initial state uncertainties, and the measurement standard deviations are given in Tables II to IV. We here note that IMU datasheet values are scaled to accommodate platform induced vibrations. The Geman-McClure M-estimator was kept close to its default GTSAM configuration for both the UWB range and BLEDAR azimuth and range, with a slightly stricter threshold value of $c = 0.9$, whilst a more lenient threshold value of $c = 3$ was used for BLEDAR elevation angle measurements. The number of outliers noticeable in Fig. 6 motivated the stricter threshold for the CS range, but the infrequent measurement rate could also be an argument for selecting a more lenient threshold, in order to ensure sufficient information available for estimation.

V. Results and discussion

The estimated range and azimuth and elevation angles from the DF and CS setup during the flight described in the previous section are shown in Fig. 6 and compared to the equivalent signal derived from RTK-GNSS. Here, we clearly observe DF and CS measurements being received simultaneously. Hence, any BLE channel collision present is not detrimental,

TABLE II
IMU PARAMETERS FOR INS.

Parameter	Value	Units
VRW	0.07	m/s/$\sqrt{\text{Hz}}$
ARW	0.15	deg/$\sqrt{\text{Hz}}$
Bias instability accelerometer	0.05	milli-g
Bias instability gyroscope	0.5	deg/hour
T_{acc}, T_{ars}	3600.0	s
g_0	9.80665	m/s^2
Accelerometer noise scaling	33.0	
Gyroscope noise scaling	100.0	
Bias scaling	5.0	

TABLE III
INITIAL STATE UNCERTAINTY.

Parameter	Value	Units
Roll and pitch	25	°
Yaw	150	°
Horizontal position	2.5	m
Vertical position	5.0	m
Velocity	0.5	m/s
Accelerometer bias	0.1	m/s^2
Angular rate sensor bias	0.5	°/s

but reducing the risk further might improve the performance and/or robustness.

One can observe a time period between 250-400 seconds[1] and one shorter period before 600 seconds without DF estimates. During the entire experiment, we have CS range estimates, but these have more outliers than the DF estimates. More DF noise can be observed between 800 and 1000 seconds. This is due to reduced SNR as a result of the reduced antenna gain at large angles away from boresight, as seen in Fig. 6. Regarding the CS range, one can observe that this has low noise when disregarding significant outliers. However, the data indicate a small, but persistent, bias in the range estimate. This is most likely due to an additional experienced propagation distance as a result of latency inside the electronics.

As mentioned in Sections II-A and II-B both the principles and algorithms for the estimation of the DF and CS range are indirectly or directly based on the assumption of zero relative velocity between the transmitter and receiver. Nevertheless, both setups and algorithms provide estimates of direction and range with a similar mean, but more noise than the equivalent signals derived with RTK-GNSS cf. Fig. 6 during flight. Still, it would be valuable to study if any performance improvement could be made for both DF and CS if the zero-

[1]Due to a human error

TABLE IV
MEASUREMENT NOISE STANDARD DEVIATIONS.

Measurement	Value	Units
RTK-GNSS pos	1.5, 1.5, 3.0	m
BLE PARS (azimuth, elevation, range)	5, 5, 3.5	°, °, m
UWB range	1.5	m
Barometric altitude	3.0	m

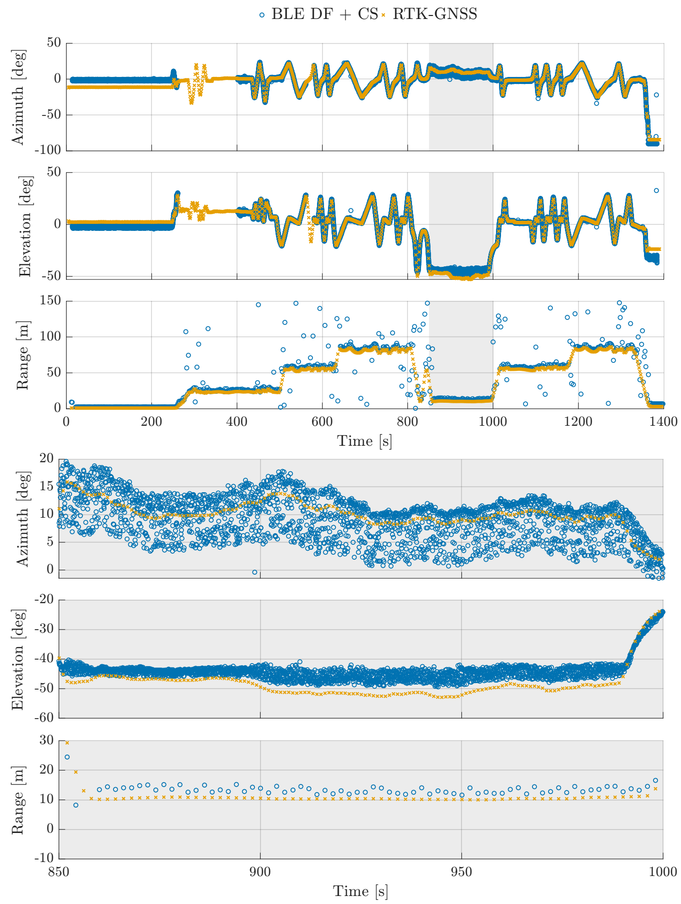

Fig. 6. **Top:** Azimuth, elevation, and range measurements from BLE Direction Finding and Channel Sounding compared to RTK-GNSS derived measurements in the multirotor experiment. **Bottom:** Zoom-in on a section with more notable noise.

TABLE V
NED POSITION RMSE COMPUTED AGAINST RTK-GNSS REFERENCE DURING $400 \leq t \leq 1375$. THE ESTIMATED POSITION USING RTK-GNSS POSITION THROUGHOUT SERVES AS A BENCHMARK.

	North [m]	East [m]	Down [m]	Norm [m]
RTK-GNSS	0.107	0.087	0.072	0.155
BLE DF+CS No robust	6.794	7.167	12.872	16.224
BLE DF+CS GmC	1.386	1.479	2.517	3.232
UWB Multilateration No robust	1.421	1.033	0.908	1.978
UWB Multilateration GmC	0.618	0.620	0.904	1.258
Barometer No robust	2.922	5.672	1.004	6.459
Barometer GmC	0.860	1.218	0.605	1.609

velocity assumption could be relaxed by using the INS velocity estimates to compensate for velocity during RF sampling.

The estimation error with uncertainty for the aiding from RTK-GNSS and BLEDAR using Geman-McClure relative to RTK-GNSS is shown in Fig. 7, whilst the RMSE statistics for RTK-GNSS and BLEDAR based INS aiding, with and without the robust Geman-McClure error function, are shown in Table V. The time interval of analysis is selected from 400s (after extended DF dropout) to 1375s (landing). One can see

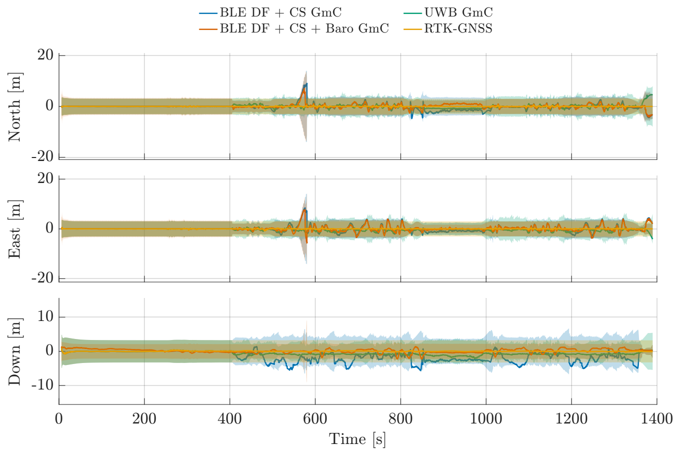

Fig. 7. NED position estimation error and 3σ-bounds (same-coloured shaded area) using BLE PARS, BLE PARS + baro, and UWB ranges to aid the INS. Both GNSS-denied INS aiding strategies use the Geman-McClure M-estimator for down-weighting measurement outliers.

from the RMSE results that the Geman-McClure cost function significantly improves the position estimation performance.

The estimation error increases during the transition from INS aiding from RTK-GNSS to PARS. This is expected since the PARS measurements have higher uncertainty and lower accuracy than RTK-GNSS and the PARS measurements also relate to the INS position more non-linearly than GNSS-RTK cf. the measurement models and Jacobians of (17) and (21).

Around 550 seconds the position error begin to oscillate more. In this time window there is a shorter time window where DF drops out at the same time as there are significant outliers in the CS range measurements available cf. Fig. 6. The result is that the position error begins to drift due to INS dead reckoning. This is also expected, but the drift in the north direction is larger in magnitude than the uncertainty estimates predict as seen in Fig. 7. The reason for this is likely a combination of coloured PARS measurement noise, non-ideal down-weighting of erroneous measurements, sub-optimal estimation of unobserved states like attitude, and sub-optimal tuning. These effects combined negatively affect the bias estimates, again exaggerating the INS drift. However, we do note that when considering the RMSE, using the robust error function largely mitigates the issues here.

Using the barometer in addition to the PARS measurements clearly improves the position estimation performance, as seen in Table V and Fig. 7. Both with and without using the robust error function significant performance gains are made here. In the time period in which DF is unavailable after RTK-GNSS handover, this is particularly evident. The drift in North direction is mainly prevented, and most of the spikes in Down-position estimate are mitigated. This may be explained by the fact that the barometric pressure provides an additional source of vertical information to the CS range, which helps stabilise the estimate when faced with the notable outliers in the latter seen in Fig. 6.

From Table V and Fig. 7 one can clearly see that the UWB-aided INS outperforms the INS aided by BLE-based PARS measurement. Given results like [37], [38] it is expected that UWB-aided INS has high-performance if the anchor geometry is good. Here, the position dilution of precision is PDOP $= \sqrt{(\mathrm{trace}((\boldsymbol{H}^\top \boldsymbol{H})^{-1})} = 1.61$ when the UAS is in position $\boldsymbol{p}_{nb}^n = [1, 1, -10]^\top$ for UWB, whilst the PDOP = 10.25 for the BLE-based PARS at the same location. These numbers are not directly comparable since PARS also uses bearing measurements, but they are still an indication of the impact of geometries on the position estimation error. The strength of PARS is still that one is able to localise with only one antenna array at one location (if one range is available). Therefore, the relative performance differences of aiding using UWB ranging vs PARS will change if the UWB geometry is worse. E.g., in a docking scenario of a vessel where there are no UWB anchors located in the sea behind the vessel when it is approaching the dock.

VI. Conclusion

This work demonstrated a fully BLE-based PARS – BLEDAR-aided inertial navigation system that fuses DF-based bearing and CS-based range measurements with IMU data in a tightly coupled approach using a factor-graph framework. The outdoor flight experiment showed that the system can bound INS drift in GNSS-denied conditions using only a single ground-based antenna array. The Geman–McClure robust cost function significantly improved performance by reducing the impact of outliers. Barometric aiding further improved the navigation system performance. Although the system does not match the accuracy of a multi-anchor UWB multiranging setup with good geometry, the results highlight the key advantage of PARS: enabling 3D positioning with minimal infrastructure. This makes the approach attractive for scenarios where multiple anchors cannot be deployed.

In the future, we will also relax the assumption that both initiator and reflector in the CS ranging are stationary using estimated velocities from the integrated navigation systems. We will also robustify the co-operability between BLE DF and CS by looking at randomised channel switching patterns and channel allocation.

Acknowledgements

The authors would like to thank colleagues Pål Kvaløy and Morten Einarsve at the Department of Engineering Cybernetics for their help in conducting field experiments with the multirotor drone.

References

[1] T. Humphreys, "Interference," in *Springer Handbook of Global Navigation Satellite Systems*, ser. Springer Handbooks, P. J. Teunissen and O. Montenbruck, Eds. Springer Cham, 2017.

[2] C. Forster, L. Carlone, F. Dellaert, and D. Scaramuzza, "On-Manifold Preintegration for Real-Time Visual–Inertial Odometry," *IEEE Transactions on Robotics*, vol. 33, no. 1, pp. 1–21, Feb. 2017. [Online]. Available: https://ieeexplore.ieee.org/document/7557075/

[3] T. Shan, B. Englot, D. Meyers, W. Wang, C. Ratti, and D. Rus, "Lio-sam: Tightly-coupled lidar inertial odometry via smoothing and mapping," in *IEEE/RSJ International Conference on Intelligent Robots and Systems (IROS)*, Las Vegas, USA, 2020.

[4] K. Gryte, T. H. Bryne, and T. A. Johansen, “Unmanned aircraft flight control aided by phased-array radio navigation,” *Journal of Field Robotics*, vol. 38, no. 4, pp. 532–551, 2021.
[5] M. Okuhara, T. H. Bryne, K. Gryte, and T. A. Johansen, “Elevation Angle Redundancy from Barometric Altitude in Multipath-affected Phased Array Radio Navigation of UAVs,” in *2024 International Conference on Unmanned Aircraft Systems (ICUAS)*. Chania - Crete, Greece: IEEE, Jun. 2024, pp. 1117–1124. [Online]. Available: https://ieeexplore.ieee.org/document/10557018/
[6] H. L. Van Trees, *Optimum Array Processing: Part IV of Detection, Estimation, and Modulation Theory*. New York, USA: John Wiley and Sons, Inc., 2002.
[7] P.-J. Chung, M. Viberg, and J. Yu, “DOA Estimation Methods and Algorithms,” in *Academic Press Library in Signal Processing: Volume 3*, ser. Academic Press Library in Signal Processing, A. M. Zoubir, M. Viberg, R. Chellappa, and S. Theodoridis, Eds. Elsevier, 2014, vol. 3, pp. 599–650. [Online]. Available: http://www.sciencedirect.com/science/article/pii/B978012411597200014X
[8] M. A. Al-Sadoon, N. T. Ali, Y. Dama, A. Zuid, S. M. Jones, R. A. Abd-Alhameed, and J. M. Noras, “A new low complexity angle of arrival algorithm for 1D and 2D direction estimation in MIMO smart antenna systems,” *Sensors (Switzerland)*, vol. 17, no. 11, 2017. [Online]. Available: https://www.mdpi.com/1424-8220/17/11/2631
[9] M. L. Sollie, T. H. Bryne, K. Gryte, and T. A. Johansen, “Reducing Ground Reflection Multipath Errors for Bluetooth Angle-of-Arrival Estimation by Combining Independent Antenna Arrays,” *IEEE Antennas and Wireless Propagation Letters*, vol. 22, no. 6, pp. 1391–1395, Jun. 2023, conference Name: IEEE Antennas and Wireless Propagation Letters. [Online]. Available: https://ieeexplore.ieee.org/document/10039075
[10] M. Wolley, “Bluetooth® Channel Sounding: A Technical Overview.” [Online]. Available: https://www.bluetooth.com/channel-sounding-tech-overview/
[11] “Bluetooth Core Specification 6.2.” [Online]. Available: https://www.bluetooth.com/wp-content/uploads/Files/Specification/HTML/Core-62/out/en/index-en.html
[12] M. Pelka, C. Bollmeyer, and H. Hellbrück, “Accurate radio distance estimation by phase measurements with multiple frequencies,” in *2014 International Conference on Indoor Positioning and Indoor Navigation (IPIN)*, Busan, Korea, Oct. 2014, pp. 142–151. [Online]. Available: https://ieeexplore.ieee.org/document/7275478/?arnumber=7275478
[13] P. Zand, J. Romme, J. Govers, F. Pasveer, and G. Dolmans, “A high-accuracy phase-based ranging solution with Bluetooth Low Energy (BLE),” in *2019 IEEE Wireless Communications and Networking Conference (WCNC)*. Marrakesh, Morocco: IEEE, Apr. 2019, pp. 1–8. [Online]. Available: https://ieeexplore.ieee.org/document/8885791/
[14] Y. Schröder, D. Reimers, and L. Wolf, “Accurate and Precise Distance Estimation from Phase-Based Ranging Data,” in *2018 International Conference on Indoor Positioning and Indoor Navigation (IPIN)*, Nantes, France, Sep. 2018, pp. 1–8, iSSN: 2471-917X. [Online]. Available: https://ieeexplore.ieee.org/document/8533871
[15] P. Boer, J. Romme, J. Govers, and G. Dolmans, “Performance of High-Accuracy Phase-Based Ranging in Multipath Environments,” in *2020 IEEE 91st Vehicular Technology Conference (VTC2020-Spring)*, Antwerp, Belgium, May 2020, pp. 1–5. [Online]. Available: https://ieeexplore.ieee.org/document/9128721/citations#citations
[16] D. Maklada, Y. Obeid-Zoabi, A. Eilam, and M. Dikshtein, “High Accuracy Distance Measurement Using Frequency Comb,” in *2021 IEEE International Conference on Microwaves, Antennas, Communications and Electronic Systems (COMCAS)*, Tel Aviv, Israel, Nov. 2021, pp. 361–366. [Online]. Available: https://ieeexplore.ieee.org/document/9629073
[17] K. Kansanen, J. A. Forbord, and J. Suárez, “Bayesian Distance Estimation with Incoherent Multi-Frequency Two-Way Phase Measurements,” in *2025 33rd European Signal Processing Conference (EUSIPCO)*, Palermo, Italy, Sep. 2025, pp. 1972–1976. [Online]. Available: https://ieeexplore.ieee.org/document/11226184/
[18] M. L. Sollie, K. Gryte, T. H. Bryne, and T. A. Johansen, “Outdoor Navigation Using Bluetooth Angle-of-Arrival Measurements,” *IEEE Access*, vol. 10, pp. 88 012–88 033, 2022. [Online]. Available: https://ieeexplore.ieee.org/document/9861605/
[19] G. H. M. Sørensen, T. H. Bryne, K. Gryte, and T. A. Johansen, “Bluetooth Phased-array Aided Inertial Navigation Using Factor Graphs: Experimental Verification,” Feb. 2026, arXiv:2602.17407 [eess]. [Online]. Available: http://arxiv.org/abs/2602.17407
[20] H. Krim and M. Viberg, “Two decades of array signal processing research: The parametric approach,” *IEEE Signal Processing Magazine*, vol. 13, no. 4, pp. 67–94, 1996.
[21] J. Wieme, R. Nietvelt, D. van Leemput, M. Weyn, P. Crombez, R. Berkvens, E. de Poorter, and J. Hoebeke, “Performance Evaluation of Bluetooth Channel Sounding on Commercial Hardware,” *IEEE Access*, vol. 13, pp. 180 862–180 876, 2025. [Online]. Available: https://ieeexplore.ieee.org/document/11207662/
[22] S. N. Shoudha, J. P. Van Marter, S. Helwa, A. G. Dabak, M. Torlak, and N. Al-Dhahir, “Reduced-Complexity Decimeter-Level Bluetooth Ranging in Multipath Environments,” *IEEE Access*, vol. 10, pp. 38 335–38 350, 2022, conference Name: IEEE Access. [Online]. Available: https://ieeexplore.ieee.org/document/9751073
[23] M. Kaess, H. Johannsson, R. Roberts, V. Ila, J. J. Leonard, and F. Dellaert, “iSAM2: Incremental smoothing and mapping using the Bayes tree,” *The International Journal of Robotics Research (IJRR)*, vol. 31, no. 2, pp. 216–235, 2012.
[24] F. Dellaert and G. Contributors, “borglab/gtsam,” May 2022. [Online]. Available: https://github.com/borglab/gtsam)
[25] J. Solà, J. Deray, and D. Atchuthan, “A micro Lie theory for state estimation in robotics,” Dec. 2021, arXiv:1812.01537 [cs]. [Online]. Available: http://arxiv.org/abs/1812.01537
[26] C. Forster, L. Carlone, F. Dellaert, and D. Scaramuzza, “IMU Preintegration on Manifold for Efficient Visual-Inertial Maximum-a-Posteriori Estimation,” in *Robotics: Science and Systems XI*. Robotics: Science and Systems Foundation, Jul. 2015. [Online]. Available: http://www.roboticsproceedings.org/rss11/p06.pdf
[27] T. Lupton and S. Sukkarieh, “Visual-Inertial-Aided Navigation for High-Dynamic Motion in Built Environments Without Initial Conditions,” *IEEE Transactions on Robotics*, vol. 28, no. 1, pp. 61–76, Feb. 2012. [Online]. Available: http://ieeexplore.ieee.org/document/6092505/
[28] L. Carlone, Z. Kira, C. Beall, V. Indelman, and F. Dellaert, “Eliminating conditionally independent sets in factor graphs: A unifying perspective based on smart factors,” in *2014 IEEE International Conference on Robotics and Automation (ICRA)*, May 2014, pp. 4290–4297. [Online]. Available: https://ieeexplore.ieee.org/document/6907483
[29] G. H. M. Sørensen, T. H. Bryne, K. Gryte, T. Synnevåg, and T. A. Johansen, “Robust phased-array radio system aided inertial navigation using factor graph optimisation,” in *2025 European Control Conference (ECC)*, Thessaloniki, Greece, Jun. 2025, pp. 1787–1794. [Online]. Available: https://ieeexplore.ieee.org/document/11186997
[30] NASA Glenn Research Center, “Earth Atmosphere Model - Metric Units,” May 2013. [Online]. Available: https://www.grc.nasa.gov/www/k-12/airplane/atmosmet.html
[31] P. Agarwal, “Robust Graph-Based Localization and Mapping,” PhD Thesis, University of Freiburg, Freiburg, Germany, 2015.
[32] Nordic Direction Finding Connectionless TX Sample. GitHub. [Online]. Available: https://github.com/nrfconnect/sdk-nrf/tree/49a39d2/samples/bluetooth/direction_finding_connectionless_tx
[33] Nordic Direction Finding Connectionless RX Sample. GitHub. [Online]. Available: https://github.com/nrfconnect/sdk-nrf/tree/49a39d2/samples/bluetooth/direction_finding_connectionless_rx
[34] Nordic Channel Sounding Samples. GitHub. [Online]. Available: https://github.com/nrfconnect/sdk-nrf/tree/49a39d2/samples/bluetooth/channel_sounding
[35] A. Simončič, G. Morano, A. Hrovat, and T. Javornik, “Optimizing Frequency Switching Pattern to Reduce Asynchronization Effect in MCPD Ranging Systems,” *IEEE Access*, vol. 13, pp. 169 791–169 811, 2025. [Online]. Available: https://ieeexplore.ieee.org/document/11180874/
[36] F. L. Markley, “Attitude determination using vector observations: A fast optimal matrix algorithm,” in *NASA Goddard Space Flight Center*, Feb. 1993, nTRS Author Affiliations: NASA Goddard Space Flight Center NTRS Document ID: 19930015542 NTRS Research Center: Legacy CDMS (CDMS). [Online]. Available: https://ntrs.nasa.gov/citations/19930015542
[37] M. Hamer and M. W. Mueller, “An Invariant Extended Kalman Filter for IMU-UWB Sensor Fusion,” *IEEE Robotics and Automation Letters*, vol. 3, no. 3, pp. 2667–2674, 2018.
[38] F. Zhang, J. Li, X. Zhang, S. Duan, and S.-H. Yang, “Indoor Fusion Positioning Based on ”IMU-Ultrasonic-UWB” and Factor Graph Optimization Method,” *arXiv*, 2025.